Early earthquake detection capabilities of different types of future-generation gravity gradiometers

Tomofumi Shimoda, Kévin Juhel, Jean-paul Ampuero, Jean-Paul Montagner, Matteo Barsuglia

Geophysical Journal International

Geophys. J. Int. (2020) **224,** 533–542
Advance Access publication 2020 October 10
GJI Gravity, Geodesy and Tides

doi: 10.1093/gji/ggaa486

Early earthquake detection capabilities of different types of future-generation gravity gradiometers

Tomofumi Shimoda [1], Kévin Juhel [2,3], Jean-Paul Ampuero [4], Jean-Paul Montagner[2] and Matteo Barsuglia[3]

[1] *Department of Physics, University of Tokyo,* 7-3-1 *Hongo, Bunkyo-ku, Tokyo 113-0033, Japan. E-mail: shimoda@granite.phys.s.u-tokyo.ac.jp*
[2] *Université de Paris, Institut de physique du globe de Paris, CNRS, F-*75005 *Paris, France*
[3] *Université de Paris, CNRS, Astroparticule et Cosmologie, F-*75013 *Paris, France*
[4] *Université Côte d'Azur, IRD, CNRS, Observatoire de la Côte d'Azur, Géoazur, Sophia Antipolis, F-06304, France*

Accepted 2020 October 8. Received 2020 September 24; in original form 2020 May 1

SUMMARY

Since gravity changes propagate at the speed of light, gravity perturbations induced by earthquake deformation have the potential to enable faster alerts than the current earthquake early warning systems based on seismic waves. Additionally, for large earthquakes ($M_w > 8$), gravity signals may allow for a more reliable magnitude estimation than seismic-based methods. Prompt elastogravity signals induced by earthquakes of magnitude larger than 7.9 have been previously detected with seismic arrays and superconducting gravimeters. For smaller earthquakes, down to $M_w \simeq 7$, it has been proposed that detection should be based on measurements of the gradient of the gravitational field, in order to mitigate seismic vibration noise and to avoid the cancelling effect of the ground motions induced by gravity signals. Here we simulate the five independent components of the gravity gradient signals induced by earthquakes of different focal mechanisms. We study their spatial amplitude distribution to determine what kind of detectors is preferred (which components of the gravity gradient are more informative), how detectors should be arranged and how earthquake source parameters can be estimated. The results show that early earthquake detections, within 10 s of the rupture onset, using only the horizontal gravity strain components are achievable up to about 140 km distance from the epicentre. Depending on the earthquake focal mechanism and on the detector location, additional measurement of the vertical gravity strain components can enhance the detectable range by 10–20 km. These results are essential for the design of gravity-based earthquake early warning systems.

Key words: Time variable gravity; Transient deformation; Earthquake early warning.

1 INTRODUCTION

Earthquake early warning systems (EEWSs) are valuable tools for disaster risk reduction. Current systems detect earthquakes and estimate their source parameters based on the initial *P* waves, which precede the most damaging shaking carried by *S* waves (Allen & Melgar 2019). However, the promptness of current systems is limited by the fact that *P* waves, the information carrier, are less than twice as fast as *S* waves, the damage carrier: earthquake detection and alert take a substantial portion of the traveltime of the hazard, especially if seismometers are not located near the epicentre. For offshore earthquakes, the Japanese EEWS has been improved by using cabled ocean bottom seismometers, although at a high cost and difficulty of maintenance, and elsewhere the emerging technology of distributed acoustic sensing on seafloor fibre-optic cables is being explored (Sladen *et al.* 2019).

Recently a new method of earthquake early warning has been proposed that is based on 'prompt gravity signals', the transient gravity perturbations caused by the mass redistribution induced by deformation during earthquakes (Harms *et al.* 2015; Juhel *et al.* 2018). Since gravity propagates at the speed of light, prompt gravity signals are a faster messenger for earthquake detection than *P* waves. In addition, their amplitude is directly linked to the earthquake seismic moment. Therefore, gravity signals observed by future-generation high-sensitivity sensors are expected to provide a more robust early magnitude estimation than conventional seismic signals (Juhel *et al.* 2018).

Prompt elastogravity signals preceding seismic waves by 10–100 s have been detected on data recorded by superconducting gravimeters and broad-band seismometers during several large earthquakes, including the Tohoku-oki earthquake ($M_w = 9.1$; Montagner *et al.* 2016; Vallée *et al.* 2017; Vallée & Juhel 2019).

The observed signals showed good agreement with simulations (Vallée *et al.* 2017; Juhel *et al.* 2019; Zhang *et al.* 2020). These results suggested the potential of gravity measurements for EEWS. However, the capability of conventional inertial sensors, such as gravimeters and seismometers, to detect prompt gravity signals of earthquakes with magnitudes less than about 8 is almost impossible within a few tens of seconds. In fact, due to the equivalence principle, gravity changes cannot be distinguished from ground acceleration, thus background seismic noise severely challenges the detection of small-amplitude gravity signals (Heaton 2017). Moreover, gravity signals are partially cancelled by the ground accelerations they induce, especially during the initial portion of the signal (Vallée *et al.* 2017). In contrast, gravity gradiometry is not hampered by these fundamental limitations, as demonstrated in the context of gravitational wave detection (Harms 2015). Therefore, gravity gradient measurements are useful to detect earthquakes over the range of magnitudes and time scales that are critical for EEWS (Harms *et al.* 2015; Juhel *et al.* 2018).

For the purpose of earthquake detection, it is important to measure gravity gradient perturbations at frequencies around 0.1 Hz, which corresponds to the typical timescale of moderate-to-large earthquakes (few tens of seconds) and early warning (∼10 s). Several concepts of gravity gradiometers have been proposed to measure gravity gradients at such frequencies, originally in the context of low-frequency gravitational wave observation (Ando *et al.* 2010; Paik *et al.* 2016; Canuel *et al.* 2018). As explained later in Section 2.3, each detector is sensitive to different components of the gravity gradient tensor, thus their capability to detect earthquakes may be different. This is an essential consideration for the design of an actual gravity-based EEWS. Additionally, the spatial distribution of the signal amplitude is expected to depend on which components are measured, which should affect the optimal arrangement of a network of gravity-gradient detectors for EEWS.

The detectability of earthquakes of $M_w > 7$ with gravity gradiometers was assessed via simulations by Juhel *et al.* (2018), who found that the sensitivity required for prompt detections is about $10^{-15}\,\mathrm{Hz}^{-1/2}$ at 0.1 Hz. That study was limited to the two vertical-horizontal gravity gradient components, *zx* and *zy*. Here, we generalize these calculations to the gravity gradient signal induced by earthquakes for all components of the gravity gradient tensor. Based on the result, we compare the detectability of prompt gravity signals with different types of gravity gradiometers. We then analyse its dependence on the azimuth between the detector location and the earthquake epicentre, to determine the most favourable positions to install the detectors. The assumptions of the simulations are explained in Section 2. The simulation results for each component are presented in Section 3. The differences of detectability between the three gradiometer types are analysed in Section 4.

2 SIMULATION ASSUMPTIONS

2.1 Medium and source models

The gravity perturbation signal generated by a point source is calculated as the convolution of the Green's function and the source time function. To evaluate the Green's function, we assume a homogeneous half-space. The speed of *P* wave and *S* wave are set to 7.8 and 4.4 km s^{-1}, respectively, as in Juhel *et al.* (2018). We assume a buried point double-couple source with prescribed focal mechanism.

The fundamental solution for the gravity-gradient perturbation in this half-space model was derived in Harms (2016). The model is intentionally simplified: it ignores complexities such as the layering of Earth's materials, the finite size of earthquake sources, non-double-couple components, and self-gravitation. Such ingredients can be taken into account by more computationally demanding methods, such as the normal mode theory (Juhel *et al.* 2019). However, they only have second-order effects on the gravity gradient within the first few tens of seconds relevant for EEWS (Harms 2016). Thus, the simplified model adopted here is expected to provide first-order insight on the detectability of gravity perturbations.

We adopt the source time function model introduced by Juhel *et al.* (2018):

$$\dot{M}(t) = \begin{cases} a\frac{M_0}{T}(t/T)^2 & (0 < t < T) \\ a\frac{M_0}{T}\left(1-(t/T-1)^2\right)^6 & (T < t < 2T) \end{cases}, \tag{1}$$

where T is the half-duration of the rupture and $a \sim 1.48$ is a coefficient designed to satisfy $\int_0^{2T} \dot{M}_0 \mathbf{d}t = M_0$. The rupture duration is taken from the empirical relation $2T = (M_0/10^{16}\,\mathrm{N\,m})^{1/3}$ (Houston 2001). Self-similarity of the fault rupture is assumed in this model. In particular, the initial evolution ($t < T$) of the source time function is independent of the final magnitude. In the following calculations, the magnitude of the earthquake is set to $M_w = 7.0$, hence $T = 8$ s.

We investigate three representative focal mechanisms: a vertical strike-slip fault and reverse dip-slip faults with two dip angles. Their strike, dip and rake angles are (strike, dip, rake) = (0°, 90°, 0°), (180°, 10°, 90°) and (180°, 20°, 90°), respectively. The hypocentre depth is set to 20 km.

2.2 Gravity gradient tensor

The gravity gradient tensor is defined as

$$\boldsymbol{\Gamma}(\boldsymbol{x}, t) = -\boldsymbol{\nabla}\left(\boldsymbol{\nabla}\phi(\boldsymbol{x}, t)\right), \tag{2}$$

where $\phi(\boldsymbol{x}, t)$ is the gravitational potential at coordinate $\boldsymbol{x}$ and at time t. The gravity strain tensor $\boldsymbol{h}(\boldsymbol{x}, t)$ is defined as the double time integral of the gravity gradient (e.g. Harms 2015):

$$\boldsymbol{h}(\boldsymbol{x}, t) := -\int_0^t \mathrm{d}\tau \int_0^\tau \mathrm{d}\tau' \boldsymbol{\Gamma}(\boldsymbol{x}, \tau'). \tag{3}$$

Note that gravity strain is a quantity different from deformation strain. Due to the symmetry $\Gamma_{ij} = -\frac{\partial}{\partial x_i}\frac{\partial}{\partial x_j}\phi = \Gamma_{ji}$ $(i, j = x, y, z)$ and to Poisson's equation $\boldsymbol{\nabla}^2\phi = 0$ yielding $\mathrm{Tr}(\boldsymbol{\Gamma}) = 0$, both $\boldsymbol{\Gamma}$ and $\boldsymbol{h}$ have only five independent components. Here, we set the five independent components of $\boldsymbol{h}$ as depicted in Fig. 1. They are based on the radial (r), tangential (t) and vertical (z) directions relative to the epicentre and detector positions. Two horizontal components, 'plus' (+) and 'cross' (×), are defined as

$$\begin{cases} h_+ = (h_{rr} - h_{tt})/2 \\ h_\times = h_{rt} = h_{tr}, \end{cases} \tag{4}$$

which are like the shear strain and the 45° rotation of it. These two components are the measurable degrees of freedom of horizontal detectors such as the torsion-bar. Their names (plus and cross) are derived from the polarization of gravitational waves. The other three independent components are chosen to be vertical: h_{zz}, h_{rz} and h_{tz}.

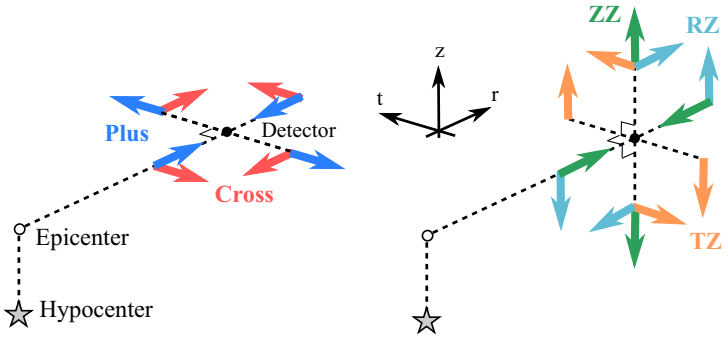

Figure 1. Definition of radial (r), transverse (t) and vertical (z) coordinates. The colour arrows show the direction of the gravitational tidal forces for each component of the gravity strain tensor.

In this paper, the perturbation of the gravitational field $\nabla\phi(\boldsymbol{x}, t)$ is computed based on the half-space model developed by Harms (2016) and the source time function model eq. (1). Then each component of the gravity gradient is approximated numerically as the finite difference of the gravity perturbations at two closely located points; for example, $\Gamma_{xy}(x, y, z, t) \simeq -\left(\frac{\partial}{\partial y}\phi(x + d/2, y, z, t) - \frac{\partial}{\partial y}\phi(x - d/2, y, z, t)\right)/d$, where $d =$ 10 m. Gravity strain $\boldsymbol{h}$ is obtained by integrating the gravity gradient twice over time as defined in eq. (3). We calculated gravity strain at various distances up to 200 or 1000 km, and various azimuths ranging from 90° to 270°. Here the azimuth angle ψ is set to 0° at the North and increases clockwise. Assuming symmetries, gravity strains at $\psi < 90°$ and at $\psi > 270°$ were inferred from the calculations at $90° < \psi < 270°$ by considering $\boldsymbol{h}(\psi < 90°,\ \psi > 270°) = \boldsymbol{h}(\psi + 180°)$ for the strike-slip event and $\boldsymbol{h}(\psi < 90°,\ \psi > 270°) = \boldsymbol{h}(180° - \psi)$ for the dip-slip events.

2.3 Proposed gravity gradiometers

Here we briefly present the three main types of low-frequency gravity gradiometers: superconducting gravity gradiometers (SGGs), torsion bar antennas and atom interferometers (AIs).

A SGG measures differential motion between levitated masses induced by fluctuations of gravity gradient. The levitated masses behave like free-falling objects, so they are sensitive to the fluctuations at low frequencies. By combining the motions of several masses, all the components of the gravity gradient tensor can be measured. Such a configuration based on six levitated masses was proposed as the SOGRO concept (Superconducting Omni-directional Gravitational Radiation Observatory; Paik *et al.* 2016, 2020), whose target sensitivity is around $10^{-19}\,\mathrm{Hz}^{-1/2}$ at 0.1 Hz with a 30-m-scale size sensor.

A torsion-bar antenna measures the relative rotations of horizontally suspended bars induced by gravity gradient perturbations. The bars have low resonant frequency about horizontal rotations. A torsion bar is mainly sensitive to the horizontal components of the gravity gradient, h_+ and $h_\times$. Although it can measure h_{rz} and h_{tz} via the vertical rotations (multi-output configuration; Shoda *et al.* 2017), we do not consider that possibility here because its sensitivity has not been well discussed yet. Two configurations, TOBA (TOrsion-Bar Antenna; Ando *et al.* 2010) and TorPeDO (Torsion Pendulum Dual Oscillator; McManus *et al.* 2017), have been proposed. TOBA is designed to achieve $10^{-19}\,\mathrm{Hz}^{-1/2}$ at 0.1 Hz with 10-m-length bars. Although a single detector with two bars is sensitive to only one component, h_+, $h_\times$ or a linear combination of them, both of the horizontal components can be measured by using two detectors with different azimuths.

An AI measures gravity field perturbations via free-falling atoms (Keith *et al.* 1991). It uses matter waves to probe the gravitational field. The components of gravity gradient measurable with AI depend on the configuration. Original configurations of AI measure vertical gravitational acceleration which directly affects the atoms, hence they are sensitive to vertical gravity gradient. The recently proposed high-sensitivity configuration MIGA (Matter wave-laser based Interferometer Gravitation Antenna; Canuel *et al.* 2018) measures the gravitational effect on horizontally propagating lasers via the atoms, hence it is sensitive to horizontal gravity gradients.

Prototypes of some of these detectors are currently under development before targeting the extreme sensitivity mentioned above ($\sim 10^{-19}\,\mathrm{Hz}^{-1/2}$) with large-scale configurations. The current best sensitivity at 0.1 Hz is $10^{-10}\,\mathrm{Hz}^{-1/2}$ achieved by an SGG (Moody *et al.* 2002). As the next step, some 1-m-scale prototype detectors are aiming for a sensitivity of about $10^{-15}\,\mathrm{Hz}^{-1/2}$ at 0.1 Hz, and worse at lower frequencies. This sensitivity target is adopted here to calculate the detectability of earthquakes by next-generation gravity-gradient instruments.

2.4 Signal-to-noise ratio of detection

Following Juhel *et al.* (2018), we consider an optimal matched-filter detection procedure. The optimal matched-filters are pre-whitened signal templates. The templates $h(t)$ are computed following the same procedure described in Sections 2.1 and 2.2 for a complete set of earthquake locations, magnitudes and focal mechanisms. Both the signal templates and the recorded data $s(t) = h(t) + n(t)$, where $n(t)$ is detector noise, are whitened by deconvolving them by the power spectrum of the detector noise. In other words, the whitened time-series $h_{\mathrm{w}}(t)$ and $s_{\mathrm{w}}(t)$ satisfy

$$h_{\mathrm{w}}(t) = \int_{-\infty}^{\infty} \frac{\tilde{h}(f)}{\sqrt{S_{\mathrm{n}}(f)}} \mathrm{e}^{2\pi \mathrm{i} f t} \mathrm{d}f, \qquad s_{\mathrm{w}}(t) = \int_{-\infty}^{\infty} \frac{\tilde{s}(f)}{\sqrt{S_{\mathrm{n}}(f)}} \mathrm{e}^{2\pi \mathrm{i} f t} \mathrm{d}f, \tag{5}$$

where $\tilde{h}(f)$ and $\tilde{s}(f)$ are the Fourier-transforms of $h(t)$ and $s(t)$ at frequency f, respectively. $S_{\mathrm{n}}(f)$ is the power spectral density (PSD) of detector noise. The matched-filter output $s_{\mathrm{mf}}(t)$ at time t is obtained by correlating the whitened template with the whitened data as

$$s_{\mathrm{mf}}(t) = \int_{-\infty}^{t} h_{\mathrm{w}}(\tau - t_0) s_{\mathrm{w}}(\tau) \mathrm{d}\tau. \tag{6}$$

Here $t = t_0$ is the time of the rupture onset. The onset is set at $\tau =$ 0 for the template $h_{\mathrm{w}}(\tau)$. The signal-to-noise ratio (SNR) is defined

as the ratio between the matched-filter output and the standard deviation of the matched-filter applied to noise alone. The SNR value is denoted $\rho(t)$ hereafter. A detection is declared if ρ exceeds a certain threshold ρ_0. Under the assumption of Gaussian detector noise, the false-alarm probability is $\mathrm{erfc}(\rho_0)$ and the detection probability is $\mathrm{erfc}(\rho_0 - \rho)$, where the complementary error function is defined as $\mathrm{erfc}(x) = \frac{1}{\sqrt{2\pi}} \int_x^\infty \mathrm{e}^{-t^2/2} \mathrm{d}t$ (eqs 1.11 and 1.12, respectively, from Chapter IV of Helstrom 1968). Here, we choose $\rho_0 = 5$ as the threshold SNR, which corresponds to a false-alarm probability of 3×10^{-7} for Gaussian noise. Note that this value underestimates the real SNR if the actual detector noise is not Gaussian. Noise statistics of the detector need to be properly characterized for a more realistic estimation of the false-alarm rate.

In this paper, the following PSD of detector noise is assumed, as in Juhel *et al.* (2018; 'model 2' noise in their fig. 1):

$$\sqrt{S_\mathrm{n}(f)} = 10^{-15} \left(1 + (f_\mathrm{c}/f)^2\right) \ \mathrm{Hz}^{-1/2}, \qquad f_\mathrm{c} = 0.1 \ \mathrm{Hz}. \tag{7}$$

The floor noise level of $10^{-15}\,\mathrm{Hz}^{-1/2}$ and the corner frequency f_c of 0.1 Hz are close to the design noise levels of proposed gravity gradiometers (Shimoda *et al.* 2020). A case study of the actual design sensitivity of TOBA is given in Supporting Information Section S1. Though the actual noise spectrum may differ in detail for each tensor component and for each type of detector, in the first-order approach taken here we assume a common noise level. For real-time application, whitening is implemented in time domain as an iterative second-order high-pass filter, namely a Butterworth filter, with 0.1 Hz cut-off frequency, whose absolute value of the frequency response turns out to be $1/\sqrt{S_\mathrm{n}(f)}$.

To evaluate the matched-filter detection performance we could draw many random realizations of noise, compute the SNR for each signal plus noise realization and average, as done by Juhel *et al.* (2018). A more efficient approach adopted here is to evaluate the following expression of the optimal SNR (Turin 1960; Jaranowski & Królak 2012):

$$\rho_\mathrm{opt}(t) = \sqrt{2 \int_{-\infty}^{\infty} \frac{|\tilde{h}_t(f)|^2}{S_\mathrm{n}(f)} \mathrm{d}f} = \sqrt{2 \int_0^t |h_\mathrm{w}(\tau)|^2 \mathrm{d}\tau} \tag{8}$$

at the detection time t (the origin of time is set at the rupture onset). Here, $\tilde{h}_t(f)$ is the Fourier transform of the template until the time t. In this paper, the optimal SNR is computed in time domain; that is, the rightmost side of eq. (8) is used, and the whitened template $h_\mathrm{w}(\tau)$ is calculated by filtering the template $h(\tau)$ with a second-order high-pass filter as mentioned above. The signal template $h(\tau)$ is prepared for each gravity strain component, each distance, and each azimuth as described in Section 2.2. The optimal SNR is achieved in the ideal case when the template used for matched-filter detection is a perfect representation of the real signal. This idealization is not severely restrictive, since prompt gravity signals depend on a smoothed version of the source time function. For example, in an unbounded space, the gravity strain signal is proportional to the fourth time-integral of the source time function (Harms *et al.* 2015). As a result, the signal is dominated by the low-frequency components of the source time function, and high-frequency fluctuations of the source have much less effect in the detection SNR.

3 SNR DISTRIBUTION FOR EACH GRAVITY GRADIENT COMPONENT

Here we show the calculated distribution of the optimal SNR $\rho_\mathrm{opt}(t)$ (eq. 8) for each component of the gravity strain tensor, calculated at two reference times: 10 s after the onset of the fault rupture and at the arrival time of *P* waves at each detector location. The former is essential for rapid detection in EEWS. Although detection before 10 s would be better, in Supporting Information Section S2 it is shown to be challenging with the proposed gravity gradiometers. The latter reference time is important for the robust estimation of earthquake source parameters such as final magnitude.

3.1 SNR at 10 s after rupture onset

Fig. 2 shows the SNR distributions at 10 s after rupture onset, at epicentral distances up to 200 km, for the three focal mechanism and the five gravity strain components. We define a 'high-SNR region' as the region where SNR >5 (inside the dashed contour), in which we can expect a reliable detection with a single detector.

The symmetry of the volumetric ground deformation produced by the different focal mechanisms, which controls the density perturbations, explains the azimuth distribution of SNR. The resulting pattern of SNR has four lobes for the strike-slip earthquake and two lobes for the dip-slip earthquakes.

For the strike-slip earthquake (left column of Fig. 2), the gravity gradient perturbation is largest in the two horizontal gravity strains, plus and cross. Their high-SNR region extends up to about 140 km from the epicentre. Only the cross strain has high SNR at azimuths 0°, 90°, 180° and 270°. The ZZ and RZ strains are also important; their SNRs are about 50 and 70 per cent of the plus strain, respectively. Though the TZ strain has the lowest SNR, in particular much lower than the cross strain, it is the only vertical gravity strain which can detect the earthquake at $\psi = 0°$, 90°, 180° and 270°.

For the dip-slip events, the vertical gravity strains are as important as the horizontal strains. The ZZ strain is dominant at 270° and the RZ strain is largest at 90°, whose high-SNR region reaches over 135 km. Among the horizontal gravity strains, the plus strain has almost the same SNR (∼95 per cent) as the ZZ strain at 270°. At the along-strike azimuths (0° and 180°), all the strains have small SNR, because the ground is not initially compressed or dilated in these directions. Only the cross and the TZ strains have detection capability in these azimuths.

As the dip angle of the dip-slip event increases from 10° to 20°, the asymmetries of the SNR distributions between the east half and the west half tend to be larger. The SNRs increase by 5–20 per cent in the azimuths of largest high-SNR region (270° for the plus and the ZZ strains, 90° for the RZ strain), and decrease significantly in the opposite directions.

3.2 SNR at *P*-wave arrival time

Fig. 3 shows the SNR distribution at *P*-wave arrival time up to 1000 km distance. In the region with SNR >100 (inside the dotted line) the signals can be measured very precisely and the earthquake source parameters can be estimated reliably. The general trends of the SNR distributions are similar to those at 10 s.

For the strike-slip event, at least two components provide good SNRs at each azimuth. The detectable region (SNR >5) extends over more than 1000 km at all azimuths. The horizontal components have the highest SNR within 350 km to the epicentre, while the SNR of the RZ strain is highest beyond 350 km distance at 45°, 135°, 225° and 315°.

For the dip-slip events, the plus, ZZ and RZ strains contribute to the detection in the along-dip directions (around 90° and 270°).

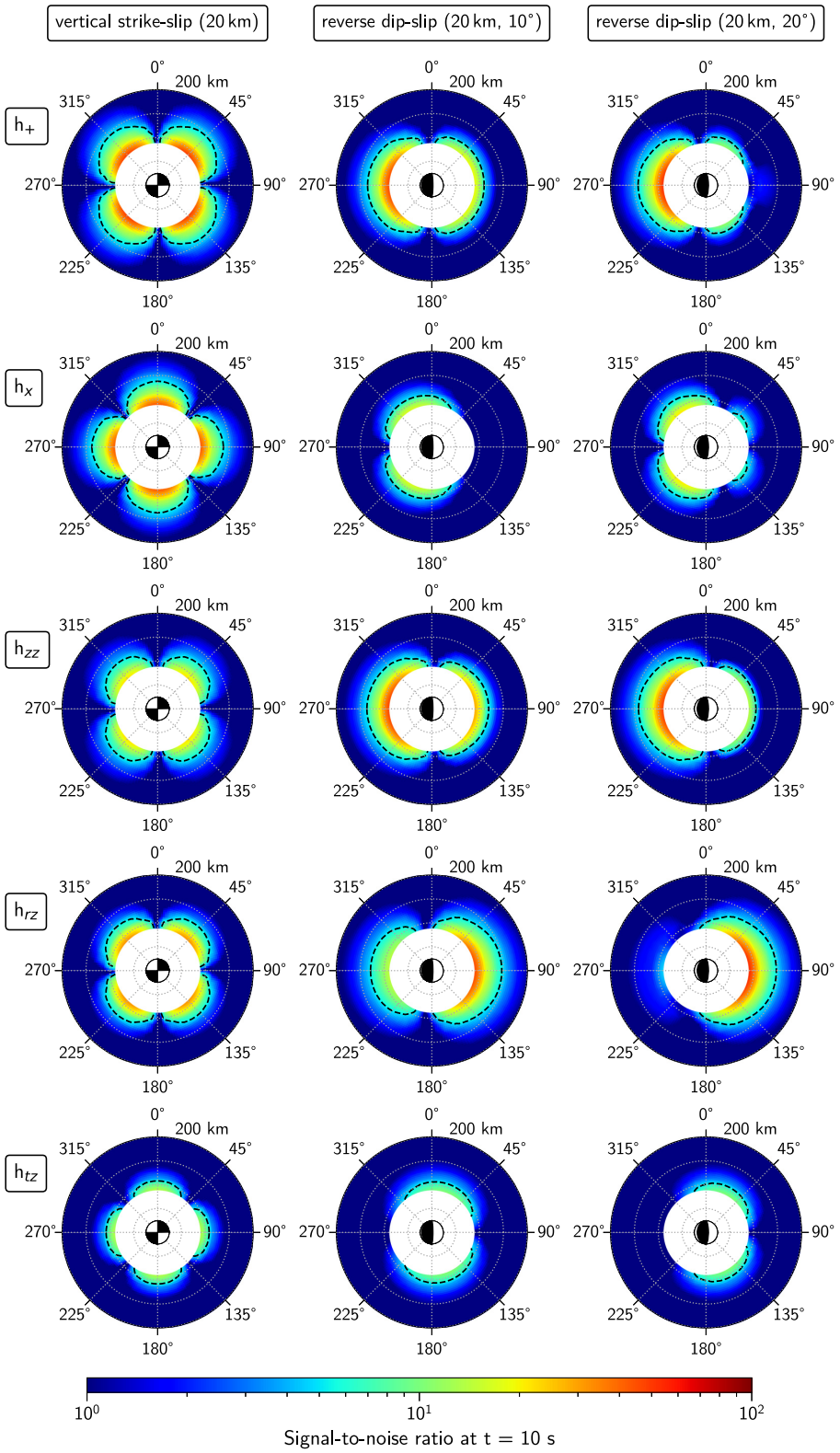

Figure 2. Azimuth–distance distributions of the SNR of matched-filter earthquake detection with gravity strain measurements at 10 s after rupture onset. The detector noise level is set to 10^{-15} Hz$^{-1/2}$ at 0.1 Hz. The magnitude is $M_w = 7.0$. Colours indicate the SNR according to the colour bar shown at the bottom. Each column corresponds to one of the three focal mechanisms mentioned in Section 2.1, and each row to one of the five components of gravity gradient tensor defined in Fig. 1. The dotted grey circles indicate distances of 50, 100 and 150 km. The dashed black curve is the contour SNR = 5. The white blank area ($\lesssim$80 km) is the region where seismic *P* waves arrive within 10 s after rupture onset.

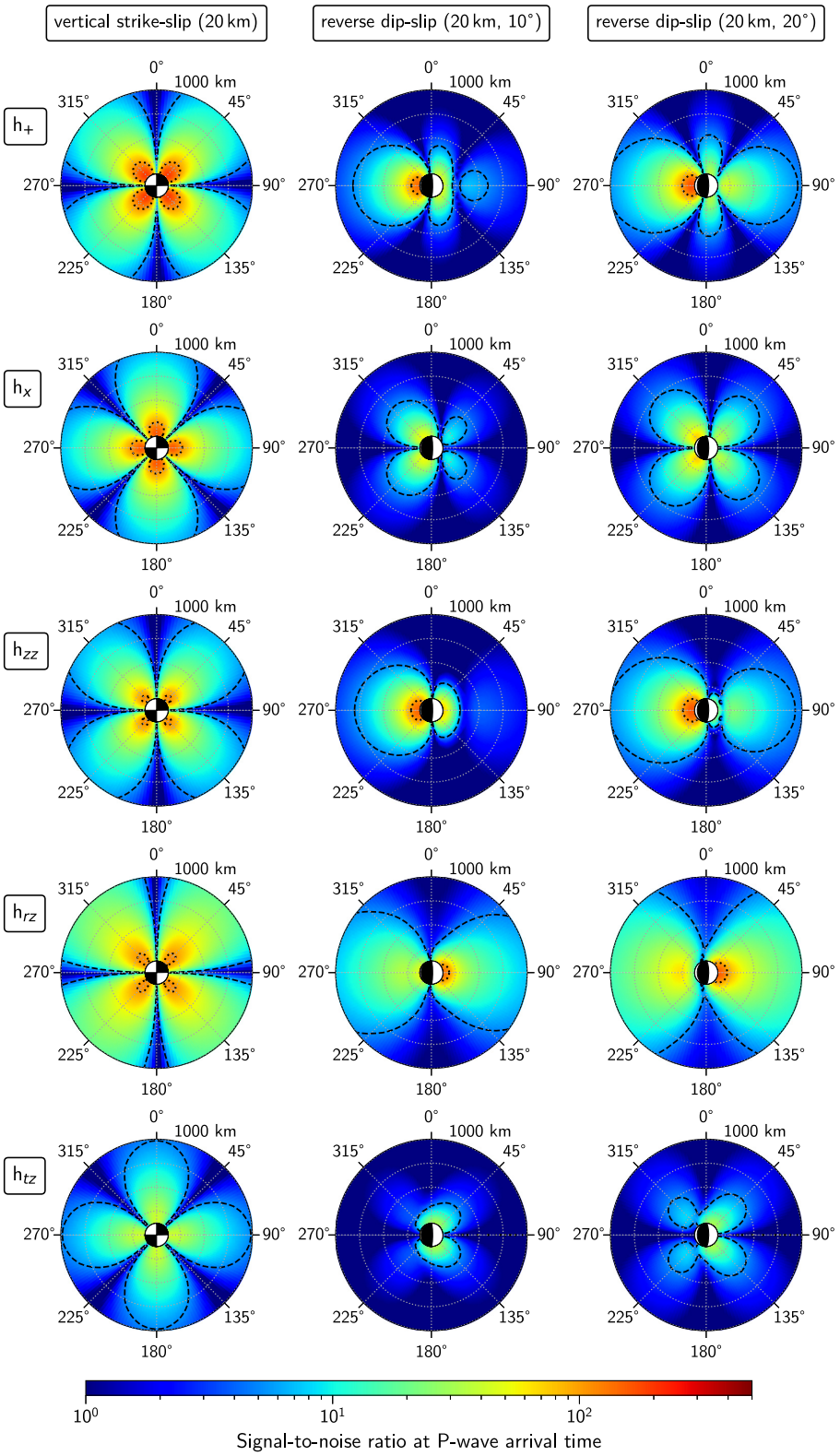

Figure 3. Same as Fig. 2 but gravity strain measurements at the *P*-wave arrival time and up to an epicentral distance of 1000 km. The magnitude is $M_w = 7.0$. The dotted grey circles indicate distances of 250, 500 and 750 km. The dashed and dotted lines are contours for SNR = 5 and 100, respectively.

However, the appropriate range for parameter estimations (SNR >100) is narrower than for the strike-slip event, while the appropriate range for detection (SNR >5) at 10 s is almost the same in the optimal directions for both type of events (Fig. 2). As the dip angle increases, the distance with SNR >100 increases at all directions except at distances <250 km. In the along-strike directions (0° and 180°), only the plus strain has a wide detectable range.

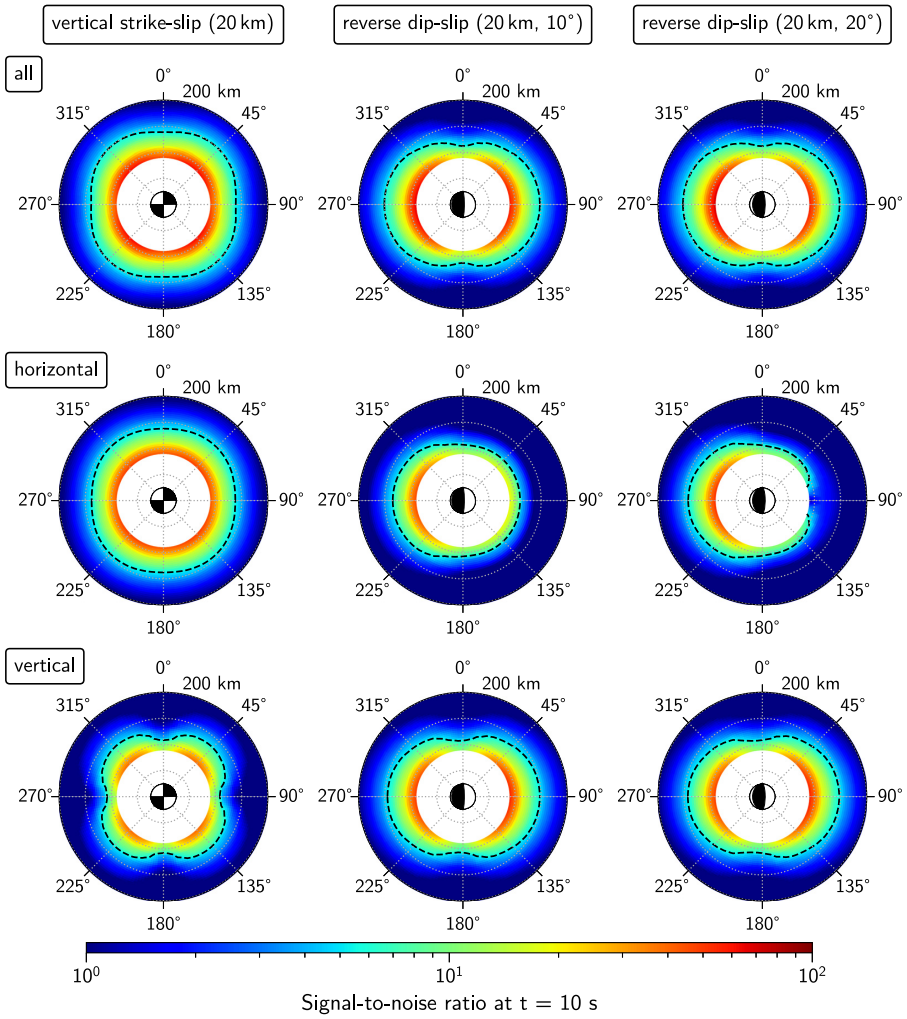

Figure 4. Total SNR for the three types of detectors at 10 s after rupture onset, up to 200 km distance. Each row corresponds to a different set of components of gravity strain: all (top), only horizontal (middle) and only vertical (bottom). The magnitude is $M_w = 7.0$.

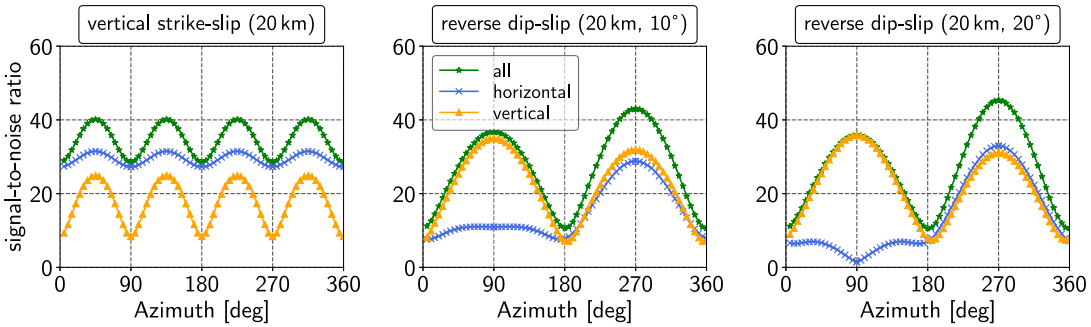

Figure 5. Azimuth distribution of total SNR at 10 s after rupture onset, at 100 km distance. The magnitude is $M_w = 7.0$.

4 SUM OF SNR FOR DIFFERENT SETS OF GRAVITY STRAIN COMPONENTS

Here, in order to assess which of the three kinds of gravity gradiometers described in Section 2.3 is preferred, we separate the horizontal set (plus and cross) and the vertical set (ZZ, RZ and TZ) of gravity strain components because some of the gradiometers are sensitive to only one of them, while an SGG like SOGRO can measure all components. The total SNR of all gravity strain components, all horizontal strains and all vertical strains are calculated by taking the square root of the sum of squares of SNRs of individual components, based on Jaranowski & Królak (2012). The detector noises in the measurements of the gravity strain components are assumed to be uncorrelated to each other. Although all the results shown in this section are the direct consequence of the previous section (Section 3), they are presented here to enable easy comparison between the types of gradiometers.

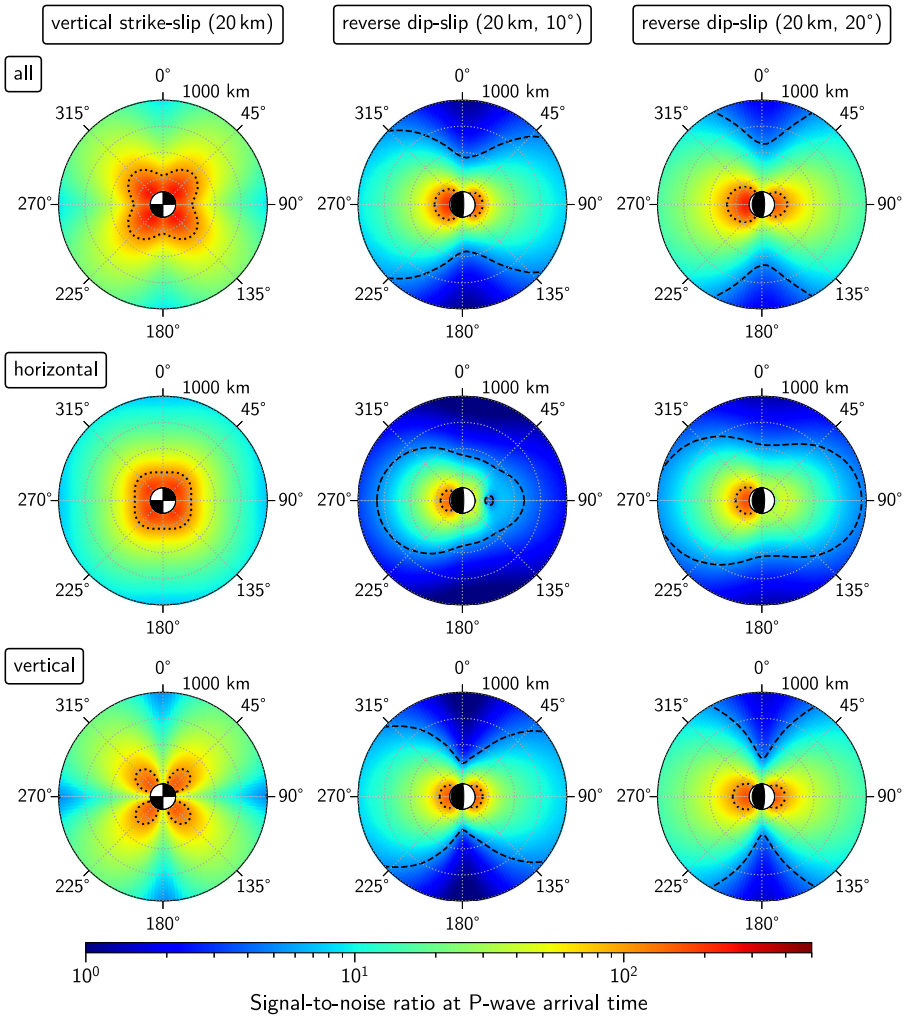

Figure 6. Total SNR for the three types of detectors at *P*-wave arrival time, up to 1000 km distance.

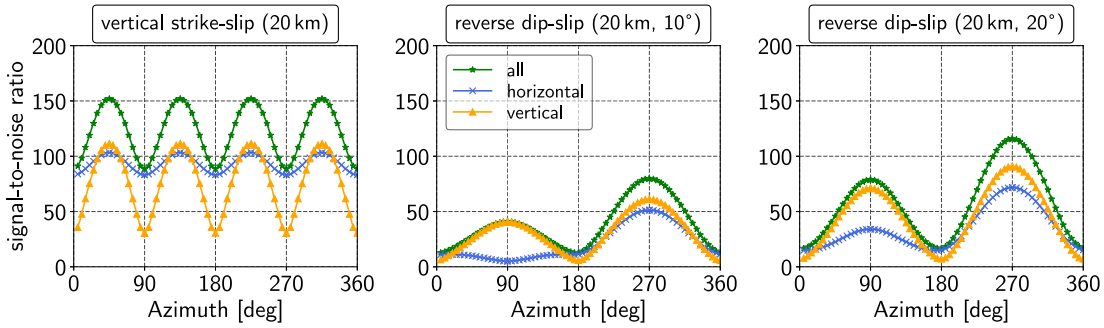

Figure 7. Azimuth distribution of total SNR at *P*-wave arrival time, at 300 km distance.

4.1 SNR at 10 s after the onset of the fault rupture

The total SNRs at 10 s after rupture onset are shown in Fig. 4. Fig. 5 shows the azimuth distribution of the SNR at 100 km distance from the epicentre.

For the strike-slip event, the total detectable range at 10 s is roughly the same at all azimuths. It is about 140–150 km for all gravity strain components and for horizontal-only components. This is because the plus and the cross strains are dominant for this event as shown in Section 3. Compared with the horizontal gravity strains, the SNR of the vertical strains is about 80 per cent at the optimal directions, while it is less than 40 per cent at the least favourable directions (Fig. 5). Adding the vertical gravity strains to the horizontal strain observation, the detectable distance is slightly improved from 145 to 150 km at 45°, 135°, 225° and 315°, but the benefit is smaller in other directions.

Thus, for strike-slip earthquakes, the horizontal components of the gravity strain perturbation are essential for rapid detection. Hence the measurement of the horizontal gravity strain, using torsion-bar detectors or AIs like MIGA, seems sufficient for EEWS. There is no preferred direction in which such detectors

should be placed, since their total SNR distribution is almost isotropic.

For dip-slip events, the detectable distance with all gravity strain components has minima in the along-strike directions (0° and 180°), because no component has very good SNR there, though the detection before the *P*-wave arrival is possible at every direction. The detectable distance for the event with 10° dip using horizontal gravity strains only is about 135 km around 270°. The set of vertical strains provides a better detectable distance of 145 km at 270°, and 150 km at 90°. As the dip angle increases from 10° to 20°, the detectable distance with the horizontal gradients slightly grows to 140 km at 270°, which is almost the same as that with the vertical strains. The SNR of the horizontal gravity strains is similar to that of the vertical strains at 270°, but much less at 90° (Fig. 5).

It should be noted that strike of dip-slip subduction thrust earthquakes is usually parallel to the coastline and detectors can only be installed on land. This corresponds to the 180°–360° azimuth range here, in which the horizontal and the vertical gravity strain have similar SNR (Figs 2–7). Prompt detection is achievable with only the horizontal gravity strain up to 135–140 km at 270°. Additional observation of the vertical gravity strain can improve the detectable distance to 150 km. Therefore, torsion-bar detectors or AIs seem sufficient for subduction earthquake detection, while SGGs like SOGRO can improve SNR by a factor $\sim \sqrt{2}$.

4.2 SNR at *P*-wave arrival time

The total SNRs at *P*-wave arrival time are shown in Fig. 6. Fig. 7 shows the SNR at 300 km distance from the epicentre.

For the strike-slip event, the observable range with the horizontal gravity strains is almost isotropic, while the vertical strains can observe earthquakes in more limited directions. For dip-slip earthquakes, the detectability strongly depends on azimuth for any sets of strain components, and the SNR is higher in the half area around 270° direction. Especially the SNR of the horizontal strains is small at 90°. The observable range of the dip-slip earthquakes is narrower than the strike-slip event, but it becomes wider as the dip angle increases.

5 CONCLUSIONS

The detectability of earthquake prompt gravity signals using different components of the gravity gradient tensor (or combinations thereof) that could be recorded by next-generation gravity gradiometers has been quantified here through simulations. The SNR of optimal matched-filter detection has been evaluated for earthquakes with magnitude M_w 7 as a function of relative position (azimuth and distance) between the sensor and the earthquake centroid, and for three different earthquake focal mechanisms.

We find that the horizontal strain components are essential for the detection of strike-slip earthquakes, and the horizontal and the vertical strain components have similar SNR for dip-slip earthquakes. Thus, a multicomponent detector like SOGRO is a better choice only if it is available with less technical difficulties than a horizontal-gradiometer like TOBA or MIGA. However, if the measurement of vertical gravity strain with SOGRO is technically difficult, it is better to use two horizontal detectors instead. The detectable range at 10 s after rupture onset with horizontal gravity strains is 140 km for strike-slip earthquakes and 135–140 km for dip-slip earthquakes. Future experimental work is necessary to determine the optimal choice of the detectors.

Our results are focused on earthquake detection, but the problem of earthquake location may bring additional constraints on the choice of gravity gradient components to measure. It has been proposed that the ratio of signal amplitude between two horizontal gravity gradient components is useful for source location (McManus *et al.* 2018). That approach can be applied more generally to the five components, which should improve the location accuracy. Therefore, observing all components of gravity strain may be important for event location, even if some do not have high SNR.

We adopted simplifying assumptions in our calculations, such as the source time function model (eq. 1) and the homogeneous half-space. For actual earthquakes, the SNR can be different than in our calculations due to the diversity of the source time functions, especially their onsets (Meier *et al.* 2017). Future work is required to address how the heterogeneities of the Earth structure may affect the gravity strain signals. However, our results provide insight on the fundamental differences between the different proposed types of gravity gradiometers. Such information is useful for the design of a gravity-based earthquake early warning system.

ACKNOWLEDGEMENTS

We acknowledge the financial support from the UnivEarthS Labex program at Sorbonne Paris Cité (ANR-10-LABX-0023 and ANR-11-IDEX-0005-02) and the Agence Nationale de la Recherche (ANR) through the grant ANR-14-CE03-0014-01. This study contributes to the IdEx Université de Paris ANR-18-IDEX-0001. TS acknowledges the financial support of GRASP (Graduate Research Abroad in Science Program) managed by University of Tokyo. JPM acknowledges the financial support of Institut Universitaire de France. JPA acknowledges funding by the French government through the 'Investissements d'Avenir UCAJEDI' project managed by the ANR through grant ANR-15-IDEX-01. We are grateful to Jan Harms for sharing his code to compute gravity changes. Numerical computations were performed on the S-CAPAD platform, IPGP, France. Python routines used to compute the expected gravity strain signal (Harms 2016) and the optimal signal-to-noise ratio are available at the GitHub repository https://github.com/kjuhel/gravity-eew. Some parts of our code make use of ObsPy package (Krischer *et al.* 2015).

REFERENCES

Allen, R.M. & Melgar, D., 2019. Earthquake early warning: advances, scientific challenges, and societal needs, *Annu. Rev. Earth Planet. Sci.,* **47**(1), 361–388.

Ando, M., Ishidoshiro, K., Yamamoto, K., Yagi, K., Kokuyama, W., Tsubono, K. & Takamori, A., 2010. Torsion-bar antenna for low-frequency gravitational-wave observations, *Phys. Rev. Lett.,* **105,** 161101, doi:10.1103/PhysRevLett.105.161101.

Canuel, B., *et al.*, 2018. Exploring gravity with the MIGA large scale atom interferometer, *Sci. Rep.,* **8**(1), 14064, doi:10.1038/s41598-018-32165-z.

Harms, J., 2015. Terrestrial gravity fluctuations, *Living Rev. Relativ.,* **18**(1), 3, doi:10.1007/s41114-019-0022-2.

Harms, J., 2016. Transient gravity perturbations from a double-couple in a homogeneous half-space, *Geophys. J. Int.,* **205**(2), 1153–1164.

Harms, J., Ampuero, J.-P., Barsuglia, M., Chassande-Mottin, E., Montagner, J.-P., Somala, S.N. & Whiting, B.F., 2015. Transient gravity perturbations induced by earthquake rupture, *Geophys. J. Int.,* **201**(3), 1416–1425.

Heaton, T.H., 2017. Correspondence: Response of a gravimeter to an instantaneous step in gravity, *Nat. Commun.,* **8**(1), 966, doi:10.1038/s41467-017-01348-z.

Helstrom, C.W., 1968. *Statistical Theory of Signal Detection,* 2ns edn, Pergamon Press.

Houston, H., 2001. Influence of depth, focal mechanism, and tectonic setting on the shape and duration of earthquake source time functions, *J. geophys. Res.,* **106**(B6), 11 137–11 150.

Jaranowski, P. & Królak, A., 2012. Gravitational-wave data analysis. Formalism and sample applications: the Gaussian case, *Living Rev. Relativ.,* **15**(1), 4, doi:10.12942/lrr-2012-4.

Juhel, K., *et al.*, 2018. Earthquake early warning using future generation gravity strainmeters, *J. geophys. Res.,* **123**(12), 10 889–10 902.

Juhel, K., *et al.*, 2019. Normal mode simulation of prompt elastogravity signals induced by an earthquake rupture, *Geophys. J. Int.,* **216**(2), 935–947.

Keith, D.W., Ekstrom, C.R., Turchette, Q.A. & Pritchard, D.E., 1991. An interferometer for atoms, *Phys. Rev. Lett.,* **66,** 2693–2696.

Krischer, L., Megies, T., Barsch, R., Beyreuther, M., Lecocq, T., Caudron, C. & Wassermann, J., 2015. ObsPy: a bridge for seismology into the scientific python ecosystem, *Comput. Sci. Discovery,* **8**(1), 014003, doi:10.1088/1749-4699/8/1/014003.

McManus, D.J., Forsyth, P.W.F., Yap, M.J., Ward, R.L., Shaddock, D.A., McClelland, D.E. & Slagmolen, B.J.J., 2017. Mechanical characterisation of the TorPeDO: a low frequency gravitational force sensor, *Class. Quantum Gravity,* **34**(13), 135002, doi:10.1088/1361-6382/aa7103.

McManus, D.J., Forsyth, P.W.F., Holland, N.A., Ward, R.L., Shaddock, D.A., McClelland, D.E. & Slagmolen, B.J.J., 2018. Early earthquake detection with a dual torsion-beam gravimeter, arXiv:1809.04787.

Meier, M.-A., Ampuero, J.P. & Heaton, T.H., 2017. The hidden simplicity of subduction megathrust earthquakes, *Science,* **357**(6357), 1277–1281.

Montagner, J.-P., *et al.*, 2016. Prompt gravity signal induced by the 2011 Tohoku-Oki earthquake, *Nat. Commun.,* **7,** 13349 EP, doi:10.1038/ncomms13349.

Moody, M.V., Paik, H.J. & Canavan, E.R., 2002. Three-axis superconducting gravity gradiometer for sensitive gravity experiments, *Rev. Sci. Instrum.,* **73**(11), 3957–3974.

Paik, H.J., Griggs, C.E., Moody, M.V., Venkateswara, K., Lee, H.M., Nielsen, A.B., Majorana, E. & Harms, J., 2016. Low-frequency terrestrial tensor gravitational-wave detector, *Class. Quantum Gravity,* **33**(7), 075003, doi:10.1088/0264-9381/33/7/075003.

Paik, H.J., Vol Moody, M. & Norton, R.S., 2020. SOGRO—terrestrial full-tensor detector for mid-frequency gravitational waves, *Int. J. Mod. Phys. D,* **29**(04), 1940001, doi:10.1142/S0218271819400017.

Shimoda, T., Takano, S., Ooi, C.P., Aritomi, N., Michimura, Y., Ando, M. & Shoda, A., 2020. Torsion-bar antenna: A ground-based mid-frequency and low-frequency gravitational wave detector, *Int. J. Mod. Phys. D,* **29**(4), 1940003, doi:10.1142/S0218271819400030.

Shoda, A., Kuwahara, Y., Ando, M., Eda, K., Tejima, K., Aso, Y. & Itoh, Y., 2017. Ground-based low-frequency gravitational-wave detector with multiple outputs, *Phys. Rev. D,* **95,** 082004, doi:10.1103/PhysRevD.95.082004.

Sladen, A., Rivet, D., Ampuero, J.P., De Barros, L., Hello, Y., Calbris, G. & Lamare, P., 2019. Distributed sensing of earthquakes and ocean-solid earth interactions on seafloor telecom cables, *Nat. Commun.,* **10**(1), 5777, doi:10.1038/s41467-019-13793-z.

Turin, G., 1960. An introduction to matched filters, *IRE Trans. Inf. Theory,* **6**(3), 311–329.

Vallée, M. & Juhel, K., 2019. Multiple observations of the prompt elastogravity signals heralding direct seismic waves, *J. geophys. Res.,* **124**(3), 2970–2989.

Vallée, M., Ampuero, J.P., Juhel, K., Bernard, P., Montagner, J.-P. & Barsuglia, M., 2017. Observations and modeling of the elastogravity signals preceding direct seismic waves, *Science,* **358**(6367), 1164–1168.

Zhang, S., Wang, R., Dahm, T., Zhou, S. & Heimann, S., 2020. Prompt elasto-gravity signals (PEGS) and their potential use in modern seismology, *Earth planet. Sci. Lett.,* **536,** 116150, doi:10.1016/j.epsl.2020.116150.

SUPPORTING INFORMATION

Supplementary data are available at *GJI* online.

Figure S1 Design sensitivity of 35-cm-scale torsion-bar antenna (Shimoda *et al.* 2020). The amplitude spectral density of the detector noise in unit of gravity strain (blue line), and the whitened noise to calculate the SNR (green line). The model sensitivity (eq. 7, red line) is also shown for comparison.

Figure S2 Azimuth–distance distributions of SNR using 35-cm-scale TOBA at 10 s after the onset of the fault rupture. Sum of the SNRs of two horizontal gravity strain components is shown in each colour map.

Figure S3 Azimuth–distance distributions of SNR using 35-cm-scale TOBA at the *P*-wave arrival time of each point. Sum of the SNRs of two horizontal gravity strain components is shown in each colour map.

Figure S4 Azimuth–distance distributions of SNR at 5 s after rupture onset. Inside the white area ($\lesssim$45 km) seismic *P* waves arrive within 5 s. The other assumptions are the same as in Fig. 2.

Please note: Oxford University Press is not responsible for the content or functionality of any supporting materials supplied by the authors. Any queries (other than missing material) should be directed to the corresponding author for the paper.